Full Length Article

Ammonia borane-based targets for new developments in laser-driven proton boron fusion

Antonino Picciotto [a,*], Matteo Valt [a,*], Daniel P. Molloy [b,c], Andrea Gaiardo [a],
Alessandro Milani [d], Vasiliki Kantarelou [e], Lorenzo Giuffrida [e], Gagik Nersisyan [b],
Aaron McNamee [b], Jonathan P. Kennedy [b], Colm R.J. Fitzpatrick [b], Philip Martin [b],
Davide Orecchia [d], Alessandro Maffini [d], Pietro Scauso [a], Lia Vanzetti [a],
Ion Cristian Edmond Turcu [f,g], Lorenza Ferrario [a], Richard Hall-Wilton [a], Daniele Margarone [b,e]

[a] Sensors and Devices Centre, Bruno Kessler Foundation, Trento 38123, Italy
[b] Centre for Light-Matter Interactions, School of Mathematics and Physics, Queen's University Belfast, Belfast BT7 1NN, Northern Ireland, UK
[c] HB11 Energy Holdings Pty, Freshwater, NSW 2096, Australia
[d] Department of Energy, Politecnico di Milano, via Ponzio 34/3, Milano 20133, Italy
[e] ELI Beamlines Facility, The Extreme Light Infrastructure ERIC, Dolní Břežany, Czech Republic
[f] UKRI/STFC Central Laser Facility, Rutherford Appleton Laboratory, Harwell Science & Innovation Campus, Didcot OX12 8HE, UK
[g] Extreme Light Infrastructure: Nuclear Physics (ELI-NP), Reactorului Street, No. 30, Magurele-Bucharest 077125, Romania

ARTICLE INFO

ABSTRACT

Nuclear fusion reactions involving protons and boron-11 nuclei are sparking increasing interest thanks to advancements in high-intensity, short-pulse laser technology. This type of reaction holds potential for a wide array of applications, from controlled nuclear fusion to radiobiology and cancer therapy. In line with this motivation, solid ammonia borane samples were developed as target material for proton-boron (pB) nuclear fusion. Following synthesis and shaping, these samples were tested for the first time in a laser-plasma pB fusion experiment. An investigation campaign focusing on surface chemical/physical analysis was carried out to characterize such samples in terms of composition of B and H, precursors of the pB fusion nuclear reaction, thus having a key impact on the yield of the generated nuclear products, i.e., alpha particles. A follow-up experiment used an 8 J, 800 fs laser pulse with an intensity of 2×10^{19} W cm^{-2} to irradiate the targets, generating $\sim 10^8$ alpha particles per steradian. The alpha particle energy range (2–6 MeV) and normalized yield per laser energy of up to (6×10^7 J/sr) are comparable with the best previous alpha particle yields found in literature. These results pave the way for a yet unexplored category of pB fusion targets.

1. Introduction

In the palette of advanced fusion concepts, the nuclear interaction between protons and boron ions stands out as a prominent and significant phenomenon. Long after its experimental discovery by Rutherford and Oliphant in the 30 s of the last century [1], proton boron fusion has been revived by the laser-plasma community since early 2000 exploiting short-pulse, high-power lasers leading to new studies enabling a deeper understanding of the underlying physics and, at the same time, an incremental optimization of the nuclear fusion reaction rate, thus triggering promising developments towards multidisciplinary applications

such as clean energy sources [2–18] and medical applications [19].

The heightened interest in this area stems from the p-^{11}B fusion reaction (p + ^{11}B → 3α + 8.7 MeV), which cross-section shows a maximum value of 1.4 barns at a kinetic energy of 675 keV of the incident proton in the laboratory frame [20,21]. A secondary resonance is also present at 160 keV with a maximum cross-section of about 0.1 barns. Then, the reaction proceeds predominantly by a sequential decay via the ground or first excited states of ^{8}Be, resulting in the production of three α particles [21]. Compared to conventional nuclear fusion reactions, e.g., deuterium–tritium fusion, the main advantage of pB fusion lies in the absence of neutrons, which implies negligible activation of potential

nuclear reactor materials, thus very low amounts of radioactive waste [2–18]. For this reason, pB fusion is considered a clean and ecologically acceptable energy production route. In addition, the kinetic energy of the produced charged products, i.e. alpha particles, could be directly converted into electricity [2–18]. After the first pB fusion pioneering experiment driven by lasers in 2005 [11], a series of promising experimental results were conducted between 2013 and 2015 [6,7,17,18] using various target materials, including boron-doped polymer (C–H + B), boron-doped silicon hydrogenated (Si-H-B), and boron nitride (B-N) targets [8–10]. These experimental studies demonstrated that, besides the characteristics of the used laser pulses, such as energy, pulse width, and intensity (W cm^{-2}), or experimental approach (e.g., "in-target" and "pitcher-catcher") schemes [4–6,8–11,17,18], a key factor for enhancing the pB fusion yield is the nature and chemical composition of the materials used as targets that should ideally contain the highest possible amount of the nuclear reaction precursors, i.e., hydrogen and boron. Following such requirements, we have designed and tested pB fusion targets made of various materials, also based on a close collaboration with scientists from the ELI Beamlines laser facility (ELI-ERIC pan-European infrastructure) and other national and international research institutions during the last 15 years, as reported in several experimental studies [4–6,8–11,17,18]. In this context, Ammonia Borane (AB), NH_3BH_3, thanks to its extremely high hydrogen capacity and stability under ambient conditions, has been acknowledged as one of the most promising candidates for pB fusion. In fact, thermolysis of AB is theoretically capable of liberating up to 19.6 wt% hydrogen (3.0 equivalents of H_2) [22,23]. In this work, we focused on the design, realization, characterization, and first test to date of AB targets as an innovative material for maximizing the number of pB fusion events using a laser-based approach. Moreover, we report a combination of radiative-hydrodynamic and particle-in-cell simulations to investigate the physics behind the laser-target interaction supporting the obtained experimental results.

2. Materials and methods

2.1. Material synthesis

Tetrahydrofuran (THF), Sodium borohydride ($NaBH_4$), Ammonium sulfate ($(NH_4)_2SO_4$) and liquid ammonia (NH_3) were purchased from VWR. All chemicals were used without any further purification. AB is produced starting from sodium borohydride and ammonium sulfate in ammoniated (5 %) THF. In a typical reaction procedure [24], liquid ammonia (5 mL) is mixed with reagent-grade THF (100 mL) contained in a flask fitted with a stirrer and Dimroth condenser. The flask was cooled in an ice-water bath. Sodium borohydride (3.783 g) and powdered ammonium sulfate (13.2 g) were transferred to the reaction flask after the addition of ammonia. The mixture was stirred carefully for 2 h at 0 °C and then at room temperature for 8 h. Subsequently, ammoniated THF solution (50 mL, 1 M) was added to the reaction mixture and stirred for 30 min. The sodium sulfate that is produced is filtered through a sintered glass crucible and then washed with THF. Obtaining a clear, transparent solution in which AB is dissolved. Finally, the filtrate was concentrated via rotary evaporation under vacuum to obtain the simplest molecular boron-nitrogen-hydride compound that appears as a white solid powder.

2.2. Material characterization

Scanning electron microscopy experiments were carried out using a SEM Phenom XL. The instrument is equipped with an EDS X-ray microanalysis system that allows the chemical analysis of the sample. In addition, the instrument is equipped with a 3D reconstruction software package capable of mapping the surface roughness of an area of 800 × 800 μm^2.

The mean surface roughness was measured utilizing a KLA-Tencor P-

6 stylus profilometer. The sampled area was 800 × 200 μm^2.

FTIR spectra were acquired in transmission mode by a micro-FTIR Nicolet iN10 equipped with a liquid nitrogen-cooled mercury cadmium telluride (MCT) detector. Samples were scanned in the range 750–4000 cm^{-1} with a 4 cm^{-1} resolution. The sampled area was 150 × 150 μm^2.

XPS measurements were performed using a Kratos AXIS UltraDLD instrument equipped with a hemispherical analyzer and a monochromatic Al Kα (1486.6 eV) X-ray source in spectroscopy mode. The AB samples were analyzed with a take-off angle between the analyzer axis and the normal to the sample surface of 0°, corresponding to a sampling depth of approximately 10 nm. The spectra were aligned, setting C 1 s core level hydrocarbon peak at 285 eV. All XPS data were analyzed using the software described in Speranza and Canteri [25].

3. Results and discussion

3.1. Compositional and surface characterization of ammonia borane targets

AB is synthesized via ammonia-mediated synthesis at ambient temperature and pressure according to the following reaction [24].

$$2NaBH_4 + (NH_4)_2SO_4 \xrightarrow{\text{5\% } NH_3 \text{ in THF}} 2NH_3BH_3 + Na_2SO_4 + 2H_2 \qquad (1)$$
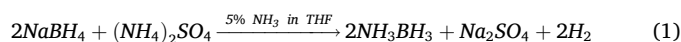
Upon completion of the reaction, 0.3 g of the synthesized powder was pressed using a pneumatic press at 5000 psi for 1 min under a low vacuum of 200 Pa.

After the pressing process, the resulting pellets had a mass of approximately 0.3 g with cylindrical symmetry and dimensions of 12 mm diameter x 2.8 mm thickness. The final density of the pellet reached a value of 0.87 g cm^{-3}. Fig. 1a shows the schematization of the process alongside a picture of the final pellet.

The morphological and chemical composition of the produced material was analyzed using SEM-EDX spectroscopy (Fig. 1b). The AB target was mainly composed of Nitrogen (46.2 atomic%) and Boron (43.2 atomic%) with the remaining atomic% of impurities of carbon and oxygen (Fig. 1c and Table S1). These findings confirm that the obtained compound after synthesis was AB with a marginal atomic concentration of carbon and oxygen, probably due to some residual organic solvent used during the preparation of the compound. Considering the pellet density of 0.87 g cm^{-3} and the molar mass of AB of 30.87 g mol^{-1}, the density of boron and hydrogen in the pellet is 1.7×10^{22} atoms cm^{-3} and 1.0×10^{23} atoms cm^{-3}, respectively. In addition, the surface morphology of the produced pellet was characterized using 3D reconstruction imaging (Fig. 1d) and mechanical surface profilometry (Figure S2, Table S2), obtaining a relatively homogeneous surface profile of the final target with a mean surface roughness of 3 ± 0.2 μm.

The vibrational spectrum of AB has been extensively investigated through both computational and experimental approaches, allowing the identification of all the modes [26]. The Fourier Transform Infra-red (FT-IR) spectrum is reported in Fig. 1e. It is worth noting that special attention was paid to the B-N vibration and their corresponding bonds with hydrogen atoms. For example, the stretching frequency of the B-N bond is identified as a well polarized band of medium intensity at 785 cm^{-1} [26]. Moreover, B-H bonds can be identified through the presence of asymmetric B-H bend at 1164 cm^{-1} and B-H stretch at 2271–2327 cm^{-1}. Additionally, the presence of an N–H bond is confirmed by the presence of a symmetric N–H bend at 1388 cm^{-1}, N–H stretch at 3245 cm^{-1} (symmetric) and 3309 cm^{-1} (asymmetric). Finally, the asymmetrical N–H and B-H rock peak at 726 cm^{-1} confirms the correct synthesis of the ammonia borane compound.

The chemical state of AB in the newly prepared target was studied by XPS, as shown in Fig. 1f and Fig. 1g. The core level of boron, B 1 s spectrum shows a peak at a binding energy (B.E.) = 188 eV, attributed to AB composite, a peak at a B.E. = 192.5 eV due to unavoidable surface
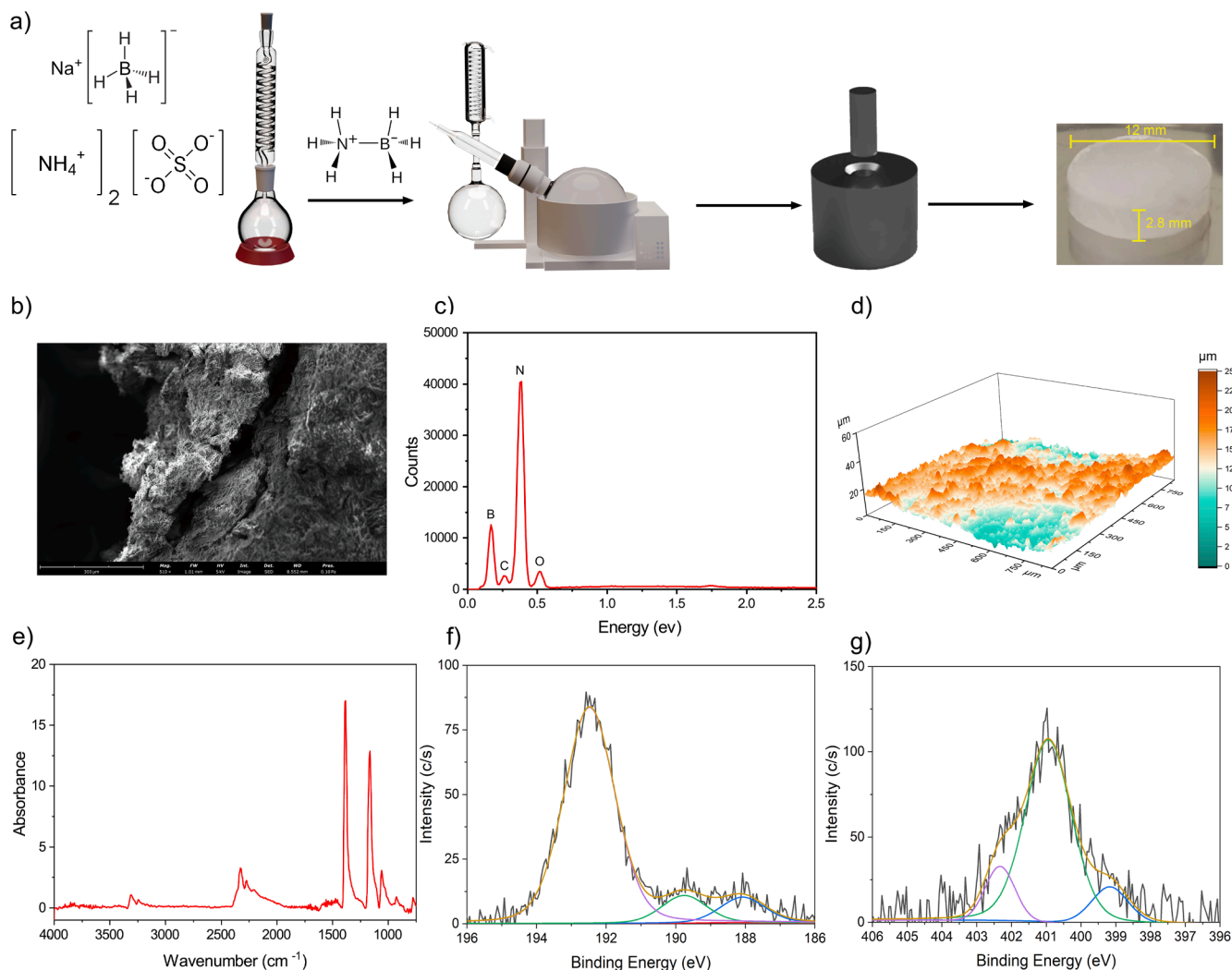
Fig. 1. A) schematic representation of the target process preparation, b) sem image on nh$_3$-BH$_3$ c) EDX analysis, d) 3D reconstruction imaging, e) FTIR spectra, f) B 1 s and g) N 1 s core level XPS spectra on AB target.

oxidation of boron during manipulations and storage of the samples. Finally, a peak at B.E. = 189.5 can be attributed to borazine-like compounds [27].

The nitrogen N 1 s core level spectrum shows three main components at 399, 401, and 402 that can be assigned to borazine-like, AB, and ammonium impurities, respectively [28].

3.2. Calibration and analysis of CR-39 nuclear tracks detectors

CR-39 nuclear track (poly-allyl-diglycol-carbonate) detectors were used to detect the alpha particles produced in the proton boron reaction to discriminate them from other ions generated in the laser-plasma interaction [7,28–40].

The detectors' energy calibration can be performed by irradiating them with monochromatic ion beams at conventional accelerator facilities or using radioactive sources. The laser-driven ion beams are not monoenergetic and, therefore, cannot accurately be used as an ion source to calibrate the CR-39 detectors unless a control spectral dispersion is used. For this experiment CR39 detectors were calibrated with an ^{241}Am source [7] (additional details can be found in Supporting Information).

In the experiment at the TARANIS laser laboratory (Queen's University Belfast, UK), protons, nitrogen, boron, carbon ions (originating from surface contaminants), and alpha particles emerging from the p^{11}B

nuclear reactions were generated as a result of high-intensity laser-target interaction, and collected by the CR-39 detectors positioned inside the interaction vacuum chamber at 44°, −45° and 80° relative to the target normal, as shown in the experimental setup in Fig. 2.

After the irradiation, the CR-39 detectors were etched for 1 h in a 6.25 M NaOH solution at 70 °C. The tracks were imaged using an optical microscope with a scale of 4.85 pixels per micrometer. A set of aluminum filters, with thicknesses ranging from 6.5 μm to 20 μm, were placed in front of the CR-39 detectors. The filters served for both: (i) shielding the CR39 from the high flux of low energy heavy ions (i.e., boron, nitrogen, and carbon) produced in the interaction, thus preventing the CR39 from saturating, and (ii) allowing for an approximate calculation of the alpha particle energy spectrum. Table 1 details the thickness of each aluminum filter alongside their respective alpha particle and carbon ion cutoff energy.

3.3. Laser-driven pB fusion experiment

The 10 TW TARANIS laser system delivered 800 fs pulses with 8–10 J energy (on target) at 1053 nm [41]. The laser focal spot had a full-width-half-max (FWHM) of 5.1 μm, corresponding to a mean laser intensity of around 2x10^{19} W cm^{-2} within the FWHM at the target surface. The laser was p-polarized on the target and incident at an angle of 20° relative to the target normal.
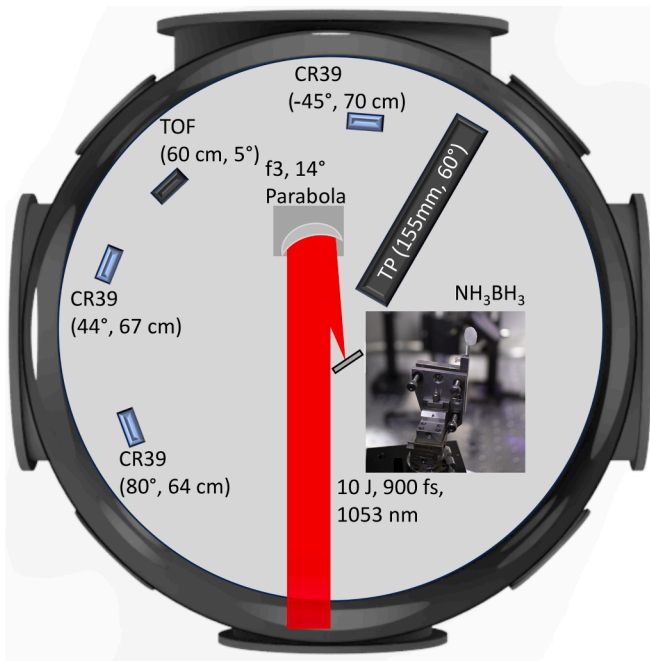
Fig. 2. Schematic of the experimental setup showing the location of the CR39 nuclear track detectors, time-of-flight diamond detector (TOF), and Thomson Parabola (TP), with an inset photo of AB target mounted on dedicated support.

Table 1

Summary of the average alpha particle flux per shot on each CR39 nuclear track detector for each thickness of Al filter placed on the CR39 and the associated ion cutoff energy of each filter thickness.

CR-39 Al filter Thickness (μm)	6.5	10	14	20
Alphas Cutoff [MeV]	2	2.8	3.7	4.8
Carbon Ion Cutoff [MeV]	7.6	11.9	16.4	22.6
YIELD @ $-45°$ [sr^{-1}]	(3.0 ± 0.2) $\cdot 10^8$	(1.5 ± 0.2) $\cdot 10^8$	(7.8 ± 2.4) $\cdot 10^6$	\
YIELD @ $44°$ [sr^{-1}]	(3.1 ± 0.4) $\cdot 10^7$	(3.5 ± 1.0) $\cdot 10^6$	(6.1 ± 3.2) $\cdot 10^6$	\
YIELD @ $80°$ [sr^{-1}]	(5.2 ± 0.1) $\cdot 10^8$	(9.9 ± 0.3) $\cdot 10^7$	(3.1 ± 0.2) $\cdot 10^7$	(2.5 ± 0.7) $\cdot 10^6$

Previous pB fusion experiments, [42], conducted at TARANIS have demonstrated that the use of H- and B-rich targets can produce pB fusion reactions through the acceleration of protons from the target front-surface (or pre-plasma) into the target bulk with energies of a few MeV, thus producing alpha particles in proximity to the target surface that are emitted in all directions but can be detected only in the backward direction of propagation due to the target thickness (forward propagating alpha particles are stopped in the bulk target).

3.4. Analysis of fusion-generated alpha particles

CR39 nuclear track detectors were positioned to observe the target front surface. Fusion-generated alpha particles and plasma ions irradiated the CR39 during the laser shot, thus producing structural damage in the CR39 material. After the chemical etching process, the damage visible in the shape of dark pits (see Fig. 3) was analyzed using an optical microscope with 50x magnification and a spatial scale of 4.85 pixels per micrometer. Using the CR39 calibration, it is possible to discriminate the fusion-generated alpha particles from the plasma ions by analyzing the pit diameter [43,44]. Aluminum filters with thickness in the range of 6.5–20 μm were used in front of each CR39 detector, allowing for the

identification and calculation of the alpha particle yield over a broad range of energies. The distances between the CR39 detectors and the AB target were 64 cm, 67 cm, and 70 cm, as shown in Fig. 2. The CR39 detectors were placed at angles from $-45°$ to $80°$, as shown in Fig. 2. Placing CR39 detectors at large angles relative to the target normal reduces the energy and flux of plasma ions, thus allowing to avoid the overlap of different particle tracks [44].

A time-of-flight (TOF) diamond detector and Thomson Parabola were placed at $5°$ and $-60°$ with respect to the target normal to detect plasma ions accelerated backward, i.e., monitor the laser-plasma interaction at each laser shot.

After the irradiation of the AB targets in the TARANIS experiment, an ex-situ analysis of the CR-39 detectors allowed estimating the flux of alpha particles generated after a certain number of laser shots during the pB fusion campaign, as summarized in Table 1. The alpha particle flux was averaged over three laser shots, and the corresponding average laser energy per shot was 8.6 J.

The alpha particle energy distributions, reconstructed thanks to the available CR39 calibration, ranged between 2 and 6 MeV, thus in good agreement with results in the literature [4–11,17,18].

The maximum recorded flux of alpha particles per laser pulse was around 5×10^8 sr^{-1} at $80°$ to target normal, which takes into account only those with energies above 2 MeV (alpha particle cutoff energy for a 6.5 μm thick Al filter). In the center-of-momentum frame, most alpha particles are generated with an energy of around 4 MeV [20,21]. Due to the relatively low energy of the protons driving the pB fusion reactions, no significant boost in alpha particle energy via momentum conservation is expected. A low alpha-particle flux of 2.5×10^6 sr^{-1} was measured at $80°$ behind a 20-μm Al filter, corresponding to alpha particles with energies above 4.8 MeV.

The measured data reported in Table 1 are also visible in Fig. 3a, 3b, and 3c with histogram graphs as yield per solid angle versus the alpha particle energy. The experimental yield of fusion events (alpha particle flux) quickly decreases when the particle energy increases.

Fig. 3a, 3b, and 3c show pictures of alpha particle tracks on CR39 detectors at different angles and related to the 6.5-μm Al filter and where it is possible to observe directly how the alpha particles population clearly shows a higher yield at $80°$ (5×10^8 sr^{-1}) compared to the other two angles ($-44°$ and $-45°$), as reported in Table 1. Using the CR39 calibration and aluminum filters up to an energy of 2–5 MeV, i.e. in good agreement with previous results on pB fusion reported previously in the in-target geometry. In addition, Fig. 4 shows a magnified raw image of one of the investigated CR39 ($80°$, 6.5 μm Al), highlighting the pits produced by the incident alpha particles. A concentration of about 50 particles has been identified over an area of 100 μm × 100 μm. The insets in Fig. 4 show two post-mortem photos of the AB target, highlighting the effect of the laser pulse impact both on the front- and rear side- a few mm-deep crater is formed after the shot.

Fig. 5 shows the proton energy distribution measured by the TOF diamond detectors in the backward direction ($5°$ relative to the target normal). The protons are accelerated backward from the target to a maximum energy of almost 3 MeV. The low energy cutoff (~ 0.6 MeV) corresponds to the energy below which the 6.5 μm Al filter stops all protons. Considering the charge-to-mass ratio of protons and (fully ionized) carbon, assuming an equivalent accelerating potential, the expected maximum energy of boron, nitrogen, and carbon ions is less than ~ 1.4 MeV/nucleon. Therefore, the 14 μm Al filter shielding the CR39 should stop even the most energetic heavy plasma ions. However, in practice, due to their higher charge-to-mass ratio, protons are accelerated on shorter timescales, shielding and effectively reducing the accelerating potential experienced by the heavier ions [45–47].

2D cartesian radiative-hydrodynamic and particle-in-cell (PIC) simulations were employed to model the intense laser interaction with the AB target, using the FLASH [48,49] and WarpX [50,51] codes, respectively. The TARANIS laser has a nanosecond contrast ratio of $\sim 5\times10^{-7}$ relative to the main picosecond-laser pulse, contributing to significant
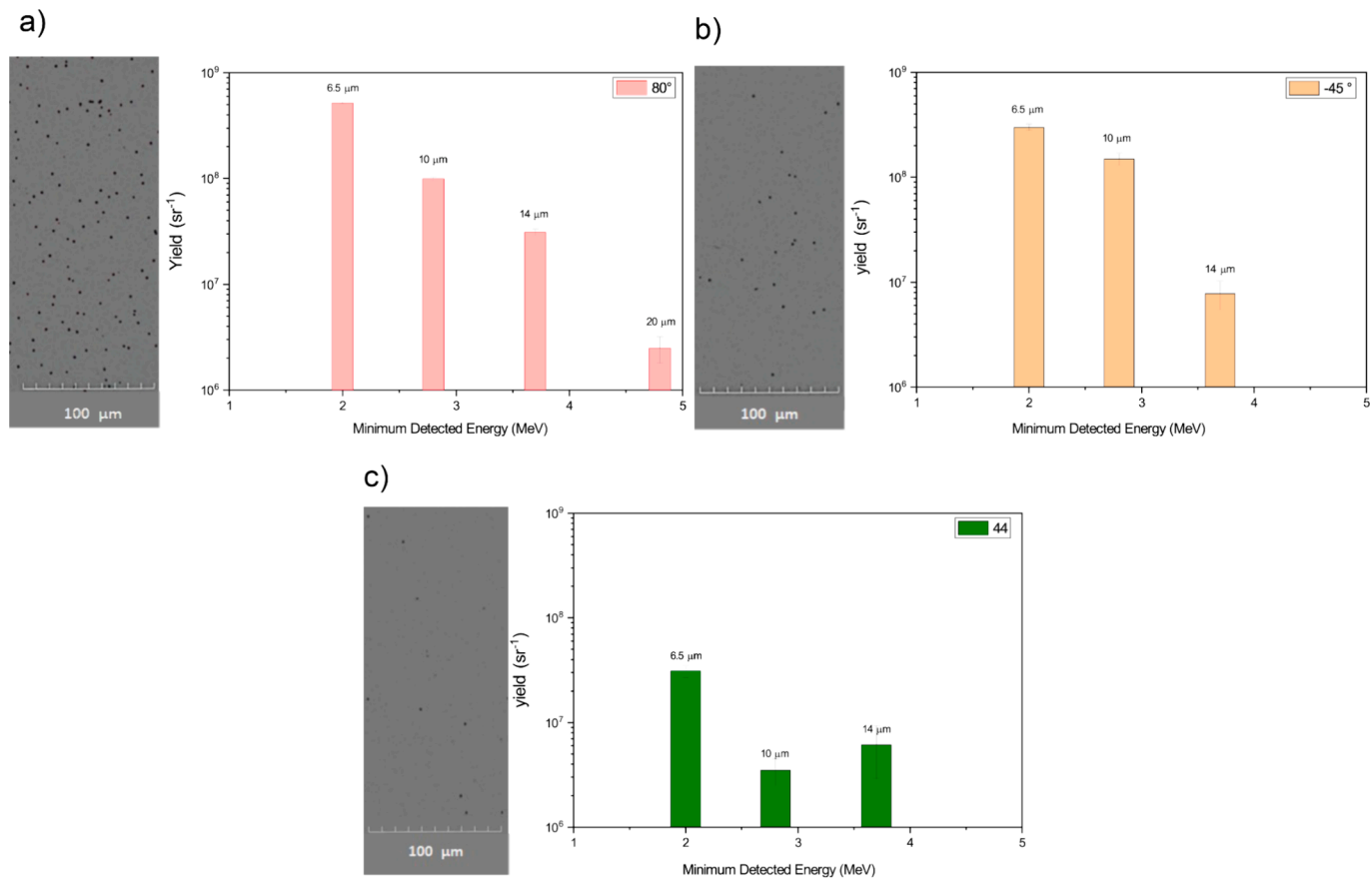
Fig. 3. A) alpha particle yield per solid angle vs particle energy at 80° relative to the target normal. b) cr-39 nuclear track detectors image of alpha particle tracks (circular black spots) at−45° c) Alpha particle yield per solid angle vs particle energy at 44°.
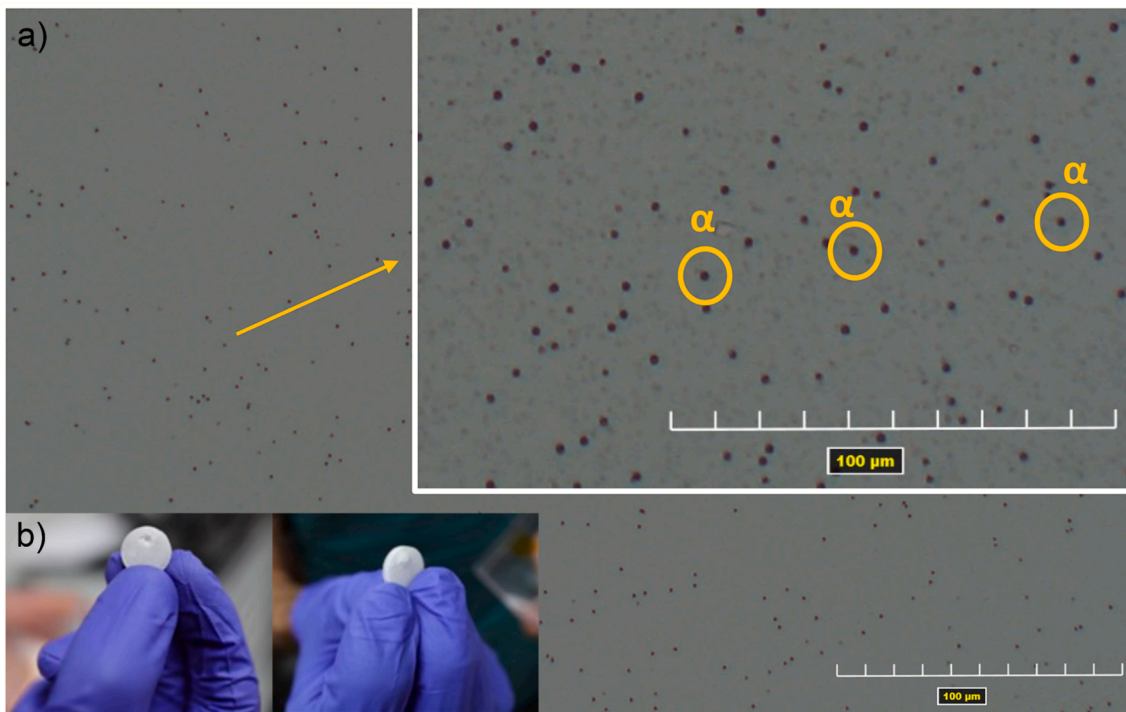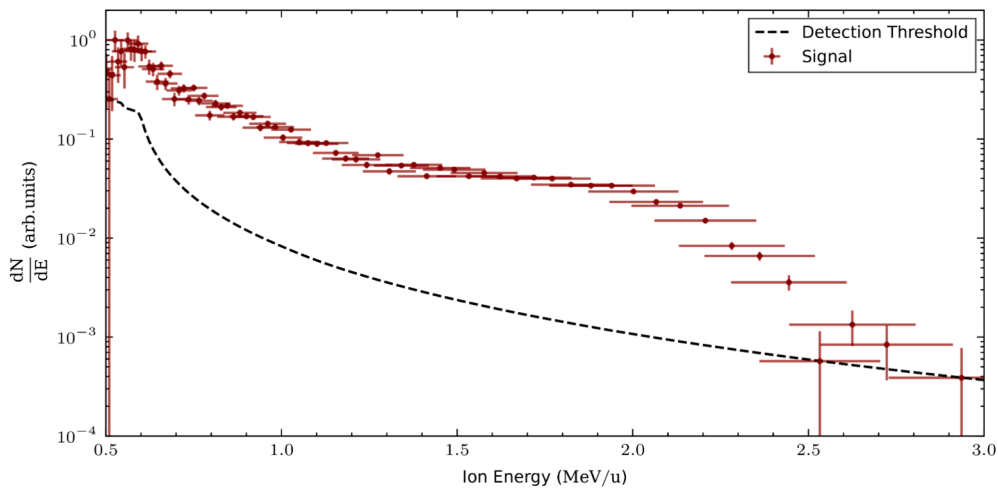

Fig. 4. A) cr-39 zoom image with the alpha particle tracks in evidence (black dark spots). b) front side and rear side of the ab target after the laser shot.

Fig. 5. Proton energy distribution per solid angle from NH_3-BH_3 target at 5° to target normal in the backward direction (not responsible for pB fusion inside the target bulk), extrapolated from time of flight (TOF) measurements, under the assumption that there is a negligible signal from heavy ions.

pre-plasma formation before the arrival of the main pulse. Using FLASH, a 1.5 ns pulse containing 7.5 mJ of energy was directed on a uniform AB target at an angle of 20° relative to the target normal simulated, and the evolution of the target density was tracked. Although the AB pellet has a surface roughness of a few micrometers over the area of a focal spot (~25 μm²), the target is approximately uniform. The equation-of-state and opacity data corresponding to NH_3-BH_3 were obtained using the FEOS code [52] and TOPS database [53], respectively. The density profile, presented in Fig. 6, corresponds to the ion and electron density along the target normal at the end of the FLASH simulation, following irradiation of the AB by the 1.5 ns pedestal. The density profile shows the generation of an extended under-dense (i.e., the electron density is less than the critical density, $\sim 10^{21}$ cm^{-3} for the TARANIS laser wavelength) pre-plasma generated from the ablated target. The scale length pre-plasma generated has a 1.8 ± 0.3 μm at the critical surface which can enhance the acceleration via the hole-boring mechanism [54]. The

ns-pedestal also drives a shock into the target, increasing the target's density by 25 % in the first $\sim$ 10 μm of the over-dense region. The density profile resulting from the FLASH radiative-hydrodynamic simulation was injected into the WarpX PIC simulation to set the initial ion and electron density. The PIC simulation modeled the interaction of the main pulse (2×10^{19} W/cm², 800 fs, 1053 nm). To reduce the computational requirements, the density was capped at half solid density, corresponding to a peak electron density of $\sim$ 160 n_c (electron critical density). However, this is still sufficient to model the hole-boring dynamics for the TARANIS laser characteristics correctly [55]. The simulation domain was composed of cells of size 15 nm x 15 nm. The particle per cell was set to have at least 1 microparticle per cell per unit of critical density for each species.

The protons were primarily accelerated forward from the critical density surface of the target via hole-boring radiation-pressure-acceleration [56,57]. Protons are also accelerated throughout the under-
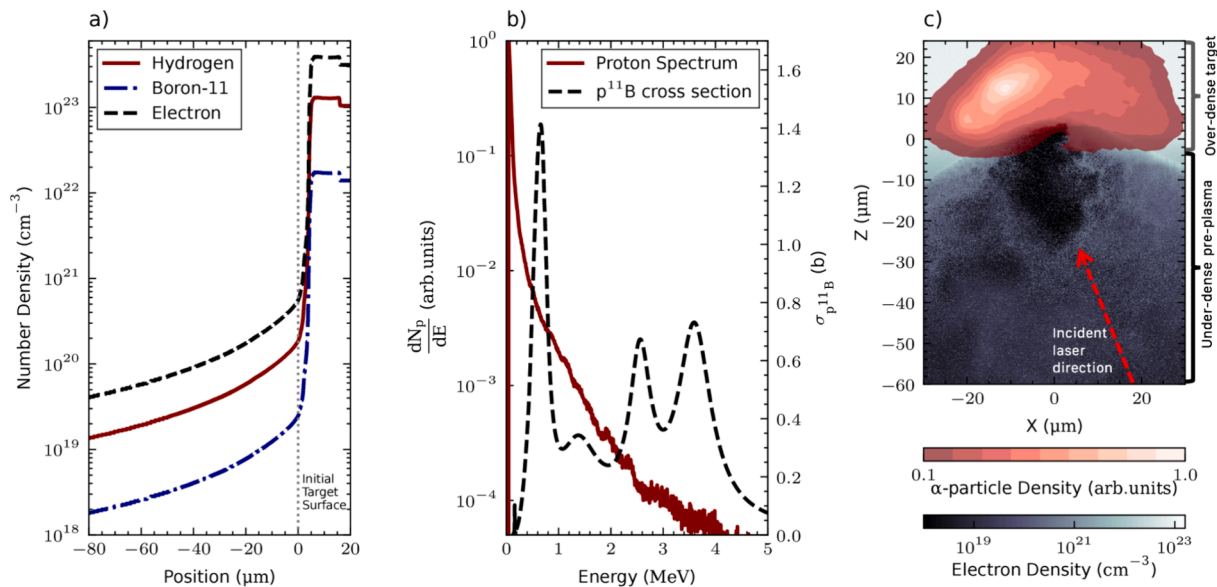
Fig. 6. A) density distribution of hydrogen, boron, and electrons along the target normal axis after the 1.5 ns pedestal modeled in FLASH before the arrival of the main laser pulse. The position of the initial target surface is displayed annotated. b) The normalized energy distribution of protons accelerated forward into the ammonia borane target, extracted from the 2D particle in cell simulation. The cross-section of the proton-boron 11 fusion cross-section over the same energy range. c) A colormap of the electron density overplotted by the distribution of fusion-generated alpha particles 1.5 ps after the peak of the laser pulse, highlighting that the majority of p^{11}B fusion reactions occur near the surface of the target.

dense plasma orthogonal to the laser propagation direction. This acceleration is attributed to the generation of a channel of low electron density as the ponderomotive force radially displaced the electrons along the laser axis, resulting in radial accelerating fields [46,58,59]. Similar mechanisms were observed in simulations modeling a laser-plasma interaction with similar laser parameters (both contrast ratio and intensity) to the TARANIS laser system [60]. The energy distribution of protons accelerated forwards into the bulk ammonia borane target, presented in Fig. 6), was retrieved from the PIC simulation. Considering Fig. 6b), using TARANIS laser parameters, it is possible to accelerate protons with energies up to a cut-off energy of ~ 4 MeV. A significant number of protons have energies above the resonance peaks of the $p^{11}B$ cross section at 170 keV and 670 keV. Therefore, it is possible to drive $p^{11}B$ fusion reactions efficiently. In the 2D PIC simulation, the backward accelerated protons have a maximum cutoff energy per nucleon ~ 4 times greater than the boron ions. Considering the TOF spectrum in Fig. 5, we can estimate the maximum heavy ion energy as ~ 0.7 MeV/nucleon, which will be stopped by the 10 μm Al foil and is on the limit of what can be stopped by the 6.5 μm Al filter. Therefore, when considering our interaction conditions, we expect a negligible number of particle tracks due to boron, carbon, etc., compared to the alpha particle flux in the filtered regions of the CR39. The WarpX PIC code can model binary collisions during the PIC cycle based on the algorithm described in [61], enabling the generation of alpha particles via $p^{11}B$ fusion. This enables us to investigate where $p^{11}B$ fusion occurs in the target. Fig. 6c) presents the spatial distribution of alpha particles generated during the WarpX PIC simulation, plotted on top of the electron density 1.5 picoseconds after the peak laser intensity. For clarity, where the alpha particle density was less than 10 % of the maximum, this was excluded from the figure. Most alpha particle generation appears to occur within the solid density region of the AB target, with negligible alpha generation occurring in the pre-plasma. However, this is expected as the density of boron in the pre-plasma (Fig. 6a) is orders of magnitude less than the solid target density. As the alpha particles are generated within the first few micrometers of the target surface and have an energy of a few MeV when generated in the in-target scheme [4], a significant fraction of alpha particles can escape from the front surface of the target and are detected by the CR39 nuclear track detectors. The density of alpha particles peaks in the direction of laser propagation. This is due to the high flux of protons that are accelerated in the direction of laser propagation from the critical surface by hole-boring acceleration. Meanwhile, the alpha generation in the X > 0 region (top right of the colormap) is driven by the lower flux of protons accelerated in the pre-plasma orthogonal to the laser axis.

It is possible to estimate the alpha particle yield using the following equation:

$$N(\alpha) = 3n_B \int_0^\infty \frac{dN_p}{dE} \cdot I(E_0) dE \qquad (2)$$

Where $I(E_0)$ is,

$$I(E_0) = \int_0^{E_0} \sigma(E) \cdot \left[\frac{dE}{dx}\right]^{-1} dE \qquad (3)$$

N_α is defined as the total number of alpha particles, n_B the boron-11 concentration in the initial solid targets in cm^{-3} ($\sim 2 \times 10^{22}$), $\frac{dN_p}{dE}$ the proton energy distribution, $\sigma(E)$ the cross-section of the $p^{11}B$ reaction and $\frac{dE}{dx}$ the stopping power of protons in the target. The analytical $p^{11}B$ cross section described in [15], the stopping power of protons in cold AB, and the simulated proton energy spectrum were used to calculate an alpha particle yield. The stopping power of protons in AB was calculated using the dedx-erpa code [62], which is based on the ion-stopping model described in [63], including the Barkas [64] and Bloch [65] terms. Considering an alpha particle yield of $\sim 10^8$ sr^{-1}, based on the modeled proton spectrum, a laser-to-proton energy conversion efficiency of

almost 50 % (for protons with energies above 200 keV) would be required to generate such a yield. This is significantly above typical conversion efficiencies for example the laser-to-deuteron conversion efficiency (up to 5 %)[60] achieved using similar laser parameters to the TARANIS laser system. However, this calculation uses the stopping power of a cold AB plasma. However, when considering degeneracy effects and higher plasma temperatures [4,66,67], there is a significant reduction in stopping power, effectively increasing the value of $I(E_0)$ in Eq. (3), which can lead to a significant increase in alpha particle yield (up to almost 2 orders of magnitude depending on the plasma conditions) as discussed in [4,66]. Recent calculations presented in [68,69] also demonstrate that given a sufficiently high ion current, which could be obtainable in these laser-plasma interactions, the ions deposit enough energy to heat the target. Considering both this ion 'drag heating' and the laser directly depositing energy into the target, the target could be heated and ionized sufficiently to reduce the rate of energy loss from protons, enhancing the alpha particle yield [4,66,67]. Thus, a laser-to-proton conversion efficiency significantly lower than almost 50 % calculated above could be sufficient to generate the measured alpha particle flux.

4. Conclusions

The presented work explored the potential use of AB-based targets for laser-driven $p^{11}B$ fusion experiments. Given its simple elemental composition and high atomic density of boron (1.7×10^{22} cm^{-3}) and hydrogen (1.0×10^{23} cm^{-3}), AB aims to represent a promising candidate for laser-plasma induced proton-boron-fusion target material. Subsequently, we produced hydrogen- and boron-rich solid-density targets based on AB. The targets were extensively characterized using various morphological and chemical techniques, revealing a highly repeatable, practical, and easily scalable synthesis method for creating a new class of $p^{11}B$ fusion targets. Additionally, when using laser systems with better contrast, the microstructured surface of the targets could enhance laser absorption [70,71], leading to an increased flux of alpha particle generation. Ex-situ CR-39, nuclear track detector analysis, returned a maximum alpha particle yield of 6×10^7 sr^{-1} J^{-1} per shot at an angle of 80° relative to the target normal produced via $p^{11}B$ fusion. The results align with the current record fluxes normalized by laser energy reported elsewhere using ns-class [4] and fs-class [43] laser pulses, highlighting the suitability of ammonia borane targets for generating alpha particles via $p^{11}B$ fusion. The laser interaction with the ammonia borane target was modeled using Radiative-hydrodynamic (FLASH) and particle-in-cell (WarpX) simulations. Using the energy spectrum of protons accelerated into the AB target extracted from the particle-in-cell simulation, a laser-to-proton conversion efficiency of almost 50 % would generate approximately 10^8 alpha particles per steradian. However, this simple calculation does not consider the different stopping power experienced by ions in a laser-generated plasma compared to a solid target, which can significantly enhance the alpha particle yield [4,66,67].

In conclusion, we performed the first Proton-Boron laser-fusion experiment with this Ammonia Borane target material. We measured the fusion alpha emission flux of 6×10^7 sr^{-1} J^{-1}. This flux is comparable to the highest alpha particle yields reported in the literature. This first such experiment paves the way for this yet unexplored class of pB laser-target materials: Boranes.

CRediT authorship contribution statement

Antonino Picciotto: Writing – review & editing, Writing – original draft, Validation, Supervision, Project administration, Methodology, Conceptualization. **Matteo Valt:** Writing – review & editing, Writing – original draft, Validation, Methodology, Investigation, Data curation, Conceptualization. **Daniel P. Molloy:** Writing – review & editing, Writing – original draft, Visualization, Project administration, Methodology, Investigation, Formal analysis, Data curation. **Andrea Gaiardo:**

Writing – review & editing, Methodology, Formal analysis. **Alessandro Milani:** Writing – original draft, Investigation. **Vasiliki Kantarelou:** Writing – original draft, Formal analysis, Data curation. **Lorenzo Giuffrida:** Supervision, Formal analysis. **Gagik Nersisyan:** Methodology, Investigation. **Aaron McNamee:** Methodology, Investigation. **Jonathan P. Kennedy:** Methodology, Investigation. **Colm R.J. Fitzpatrick:** Methodology, Investigation. **Philip Martin:** Methodology, Investigation. **Davide Orecchia:** Investigation. **Alessandro Maffini:** Writing – original draft, Investigation. **Pietro Scauso:** Investigation. **Lia Vanzetti:** Validation, Investigation. **Ion Cristian Edmond Turcu:** Writing – original draft, Supervision, Conceptualization. **Lorenza Ferrario:** Funding acquisition. **Richard Hall-Wilton:** Funding acquisition. **Daniele Margarone:** Writing – review & editing, Supervision, Funding acquisition.

Declaration of competing interest

The authors declare the following financial interests/personal relationships which may be considered as potential competing interests: [Author DPM's PhD is sponsored by HB11 Energy Holdings Pty. The remaining authors declare that the research was conducted in the absence of any commercial or financial relationships that could be construed as a potential conflict of interest].

Data availability

Data will be made available on request.

Acknowledgments

Appendix A. Supplementary material

Supplementary data to this article can be found online at https://doi.org/10.1016/j.apsusc.2024.160797.

References

[1] M.L.E. Lord Oliphant, E. Rutherford, Proc. R. Soc. London. Ser. A, Contain. Pap. a Math. Phys. Character 141 (1933) 259.

[2] H.W. Becker, C. Rolfs, H.P. Trautvetter, Zeitschrift Für Phys. A at. Nucl. 327 (1987) 341.

[3] W. Nevins, R. Swain, Nucl. Fusion 40 (2000) 865.

[4] L. Giuffrida, F. Belloni, D. Margarone, G. Petringa, G. Milluzzo, V. Scuderi, A. Velyhan, M. Rosinski, A. Picciotto, M. Kucharik, J. Dostal, R. Dudzak, J. Krasa, V. Istokskaia, R. Catalano, S. Tudisco, C. Verona, K. Jungwirth, P. Bellutti, G. Korn, G.A.P. Cirrone, Phys. Rev. E 101 (2020) 013204.

[5] D. Margarone, J. Bonvalet, L. Giuffrida, A. Morace, V. Kantarelou, M. Tosca, D. Raffestin, P. Nicolai, A. Picciotto, Y. Abe, Y. Arikawa, S. Fujioka, Y. Fukuda, Y. Kuramitsu, H. Habara, D. Batani, Appl. Sci. 12 (2022) 1444.

[6] C. Labaune, C. Baccou, S. Depierreux, C. Goyon, G. Loisel, V. Yahia, J. Rafelski, Nat. Commun. 4 (2013) 2506.

[7] C. Baccou, V. Yahia, S. Depierreux, C. Neuville, C. Goyon, F. Consoli, R. De Angelis, J.E. Ducret, G. Boutoux, J. Rafelski, C. Labaune, Rev. Sci. Instrum. (2015) 86.

[8] D. Margarone, A. Morace, J. Bonvalet, Y. Abe, V. Kantarelou, D. Raffestin, L. Giuffrida, P. Nicolai, M. Tosca, A. Picciotto, G. Petringa, G.A.P. Cirrone, Y. Fukuda, Y. Kuramitsu, H. Habara, Y. Arikawa, S. Fujioka, E. D'Humieres, G. Korn, D. Batani, Front. Phys. (2020) 8.

[9] J. Bonvalet, P. Nicolaï, D. Raffestin, E. D'humieres, D. Batani, V. Tikhonchuk, V. Kantarelou, L. Giuffrida, M. Tosca, G. Korn, A. Picciotto, A. Morace, Y. Abe, Y. Arikawa, S. Fujioka, Y. Fukuda, Y. Kuramitsu, H. Habara, D. Margarone, Phys. Rev. E 103 (2021) 053202.

[10] G. Milluzzo, F. Belloni, G. Petringa, V. Scuderi, L. Giuffrida, A. Velyhan, C. Verona, A. Picciotto, M. Rosinski, R. Catalano, M. Crivellari, J. Dostal, R. Dudzak, L. Juha, J. Krasa, M. Krupka, M. Krůs, G. Lanzalone, R. Leanza, C.G. Litrico, M. Pfeizer, F. Schillaci, S. Tudisco, D. Margarone, G.A.P. Cirrone, J. Instrum. 18 (2023) C07022.

[11] V.S. Belyaev, A.P. Matafonov, V.I. Vinogradov, V.P. Krainov, V.S. Lisitsa, A. S. Roussetski, G.N. Ignatyev, V.P. Andrianov, Phys. Rev. E 72 (2005) 026406.

[12] S. Kimura, A. Anzalone, A. Bonasera, Phys. Rev. E 79 (2009) 038401.

[13] V.S. Belyaev, V.P. Krainov, A.P. Matafonov, B.V. Zagreev, Laser Phys. Lett. 12 (2015) 096001.

[14] T.A. Mehlhorn, L. Labun, B.M. Hegelich, D. Margarone, M.F. Gu, D. Batani, E. M. Campbell, S.X. Hu, B. Ramakrishna, Laser Part. Beams 2022 (2022) e1.

[15] A. Tentori, F. Belloni, Nucl. Fusion 63 (2023) 086001.

[16] S. Zhang, H. Xu, X. Xu, W. Wei, J. Ren, B. Chen, B. Ma, Z. Hu, F. Li, L. Liu, M. Yang, Z. Lai, H. Yue, J. Xiong, Z. Xu, Y. Chen, Z. Wang, Z. Zhou, L. Shi, R. Cheng, Z. Deng, W. Qi, W. Zhou, G. Zhao, B. Liu, D. Luo, D.H.H. Hoffmann, Y. Zhao, D. Batani, Laser Part. Beams 2023 (2023) e12.

[17] A. Picciotto, D. Margarone, A. Velyhan, P. Bellutti, J. Krasa, A. Szydłowski, G. Bertuccio, Y. Shi, A. Mangione, J. Prokupek, A. Malinowska, E. Krousky, J. Ullschmied, L. Laska, M. Kucharik, G. Korn, Phys. Rev. X 4 (2014) 031030.

[18] D. Margarone, A. Picciotto, A. Velyhan, J. Krasa, M. Kucharik, A. Mangione, A. Szydlowski, A. Malinowska, G. Bertuccio, Y. Shi, M. Crivellari, J. Ullschmied, P. Bellutti, G. Korn, Plasma Phys. Control. Fusion 57 (2015) 014030.

[19] G.A.P. Cirrone, L. Manti, D. Margarone, G. Petringa, L. Giuffrida, A. Minopoli, A. Picciotto, G. Russo, F. Cammarata, P. Pisciotta, F.M. Perozziello, F. Romano, V. Marchese, G. Milluzzo, V. Scuderi, G. Cuttone, G. Korn, Sci. Rep. 8 (2018) 1141.

[20] S. Stave, M.W. Ahmed, R.H. France, S.S. Henshaw, B. Müller, B.A. Perdue, R. M. Prior, M.C. Spraker, H.R. Weller, Phys. Lett. B 696 (2011) 26.

[21] M.H. Sikora, H.R. Weller, J. Fusion Energy 35 (2016) 538.

[22] T. Sano, S. Fujioka, Y. Mori, K. Mima, Y. Sentoku, Phys. Rev. E 101 (2020) 013206.

[23] H. Huang, C. Wang, Q. Li, R. Wang, Y. Yang, A. Muhetaer, F. Huang, B. Han, D. Xu, Adv. Funct. Mater. (2021) 31.

[24] P.V. Ramachandran, H. Mistry, A.S. Kulkarni, P.D. Gagare, Dalt. Trans. 43 (2014) 16580.

[25] G. Speranza, R. Canteri, SoftwareX 10 (2019) 100282.

[26] U.B. Demirci, Int. J. Hydrogen Energy 42 (2017) 9978.

[27] P. Bachmann, F. Düll, F. Späth, U. Bauer, H.-P. Steinrück, C. Papp, J. Chem. Phys. (2018) 149.

[28] S.L. Guo, B.-L. Chen, S.A. Durrani, In Handbook of Radioactivity Analysis, Elsevier, 2012, pp. 233–298.

[29] R.K. Jain, A. Kumar, B.K. Singh, Nucl. Instruments Methods Phys. Res. Sect. B Beam Interact. with Mater. 274 (2012) 100.

[30] G. Immè, D. Morelli, M. Aranzulla, R. Catalano, G. Mangano, Radiat. Meas. 50 (2013) 253.

[31] N. Sinenian, M.J. Rosenberg, M. Manuel, S.C. McDuffee, D.T. Casey, A.B. Zylstra, H.G. Rinderknecht, M. Gatu Johnson, F.H. Séguin, J.A. Frenje, C.K. Li, R. D. Petrasso, Rev. Sci. Instrum. 82 (2011).

[32] V. Kantarelou, A. Velyhan, P. Tchórz, M. Rosiński, G. Petringa, G.A.P. Cirrone, V. Istokskaia, J. Krása, M. Krůs, A. Picciotto, D. Margarone, L. Giuffrida, S. Pikuz, Laser Part. Beams 2023 (2023) e10.

[33] T.W. Jeong, P.K. Singh, C. Scullion, H. Ahmed, P. Hadjisolomou, C. Jeon, H. Yun, K.F. Kakolee, M. Borghesi, S. Ter-Avetisyan, Sci. Rep. 7 (2017) 2152.

[34] A. Malinowska, M. Jaskóła, A. Korman, A. Szydłowski, M. Kuk, Rev. Sci. Instrum. (2014) 85.

[35] K. Malinowski, E. Skladnik-Sadowska, M.J. Sadowski, Radiat. Meas. 40 (2005) 371.

[36] H.A. Khan, R. Brandt, N.A. Khan, K. Jamil, Nucl. Tracks Radiat. Meas. 7 (1983) 129.

[37] M. Seimetz, P. Bellido, P. García, P. Mur, A. Iborra, A. Soriano, T. Hülber, J. García López, M.C. Jiménez-Ramos, R. Lera, A. Ruiz-de la Cruz, I. Sánchez, R. Zaffino, L. Roso, J.M. Benlloch, Rev. Sci. Instrum. 89 (2018).

[38] J. Rojas-Herrera, H.G. Rinderknecht, A.B. Zylstra, M. Gatu Johnson, D. Orozco, M. J. Rosenberg, H. Sio, F.H. Seguin, J.A. Frenje, C.K. Li, R.D. Petrasso, Rev. Sci. Instrum. 86 (2015).

[39] D. Xiao-Jiao, T. Zhi-Xin, L. Xiao-Fei, H. Yong-Sheng, G. Shi-Lun, Y. Da-Wei, T. Xiu-Zhang, W. Nai-Yan, A, Phys. Sin. 59 (2010) 3147.

[40] Y. Zhang, H.-W. Wang, Y.-G. Ma, L.-X. Liu, X.-G. Cao, G.-T. Fan, G.-Q. Zhang, D.-Q. Fang, Nucl. Sci. Tech. 30 (2019) 87.

[41] T. Dzelzainis, G. Nersisyan, D. Riley, L. Romagnani, H. Ahmed, A. Bigongiari, M. Borghesi, D. Doria, B. Dromey, M. Makita, S. White, S. Kar, D. Marlow, B. Ramakrishna, G. Sarri, M. Zaka-Ul-Islam, M. Zepf, C.L. Lewis, Laser and Particle Beams 28 (3) (2010) 451.

[42] M. Tosca, D. Molloy, A. McNamee, P. Pleskunov, M. Protsak, K. Biliak, D. Nikitin, J. Kousal, Z. Krtouś, L. Hanykova', J. Hanuś, H. Biederman, T. Foster, G. Nersisyan, P. Martin, C. Ho, A. Mackova', R. Mikśova', M. Borghesi, S. Kar, V. Istokskaia, Y. Levy, A. Picciotto, L. Giuffrida, D. Margarone, A. Choukourov, Frontiers in Physics 2023, 11.

[43] A. Szydlowski, J. Badziak, J. Fuchs, M. Kubkowska, P. Parys, M. Rosinski, R. Suchanska, J. Wolowski, P. Antici, A. Mancic, Radiation Measurements 44 (9–10) (2009) 881.

[44] M.S. Schollmeier, J.J. Bekx, J. Hartmann, E. Schork, M. Speicher, A.F. Brodersen, A. Fazzini, P. Fischer, E. Gaul, B. Gonzalez-Izquierdo, M.M. Günther, A.K. Härle, R. Hollinger, K. Kenney, J. Park, D.E. Rivas, V. Scutelnic, Z. Shpilman, S. Wang, J. J. Rocca, G. Korn, Sci. Rep. 13 (2023) 1.

[45] J. Fuchs, Y. Sentoku, E. d'Humi'eres, T. E. Cowan, J. Cobble, P. Audebert, A. Kemp, A. Nikroo, P. Antici, E. Brambrink, A. Blazevic, E. M. Campbell, J. C. Ferná ndez, J.-C. Gauthier, M. Geissel, M. Hegelich, S. Karsch, H. Popescu, N. Renard-LeGalloudec, M. Roth, J. Schreiber, R. Stephens, H. P´epin, Physics of Plasmas 2007, 14, 5.

[46] A. Macchi, M. Borghesi, M. Passoni, Reviews of Modern Physics 85 (2) (2013) 751.

[47] A. Macchi arXiv preprint 2017. DOI: 10.48550/arXiv.1712.06443.

[48] B. Fryxell, K. Olson, P. Ricker, F.X. Timmes, M. Zingale, D.Q. Lamb, P. Macneice, R. Rosner, J.W. Truran, H. Tufo, The Astrophysical Journal Supplement Series 131 (1) (2000) 273.

[49] Flash Center for Computational Science, Flash website, https://flash.rochester. edu/site/index.shtml, accessed 01, 2024.

[50] EPC-WarpX, Warpx Github Repository, 2024, https://github.com/ECP-WarpX/ WarpX, accessed 01, 2024.

[51] L. Fedeli, A. Huebl, F. Boillod-Cerneux, T. Clark, K. Gott, C. Hillairet, S. Jaure, A. Leblanc, R. Lehe, A. Myers, C. Piechurski, M. Sato, N. Zaim, W. Zhang, J.-L. Vay, H. Vincenti, In SC22: International Conference for High Performance Computing, Networking, Storage and Analysis. IEEE, 2022 1–12.

[52] S. Faik, A. Tauschwitz, I. Iosilevskiy, Comput. Phys. Commun. 227 (2018) 117.

[53] G. A. Yuan, J., Gui, Z., and Moses, Final Report on Atomic Database Project, Argonne, IL, 2006.

[54] J. Hornung, Y. Zobus, S. Roeder, A. Kleinschmidt, D. Bertini, M. Zepf, V. Bagnoud, Nat. Commun. (2021) 12.

[55] N. Iwata, S. Kojima, Y. Sentoku, M. Hata, K. Mima, Nat. Commun. 9 (2018) 1.

[56] T. Schlegel, N. Naumova, V.T. Tikhonchuk, C. Labaune, I.V. Sokolov, G. Mourou, Physics of Plasmas 16 (2009) 8.

[57] A. Henig, D. Kiefer, M. Geissler, S.G. Rykovanov, R. Ramis, R. Hörlein, J. Osterhoff, Z. Major, L. Veisz, S. Karsch, F. Krausz, D. Habs, J. Schreiber, Phys. Rev. Lett. 102 (9) (2009) 095002.

[58] G.S. Sarkisov, V.Y. Bychenkov, V.N. Novikov, V.T. Tikhonchuk, A. Maksimchuk, S.-Y. Chen, R. Wagner, G. Mourou, D. Umstadter, Physical Review E 59 (6) (1999) 7042.

[59] K. Krushelnick, E.L. Clark, Z. Najmudin, M. Salvati, M.I.K. Santala, M. Tatarakis, A. E. Dangor, V. Malka, D. Neely, R. Allott, C. Danson, Physical Review Letters 83 (4) (1999) 737.

[60] H. Habara, K.L. Lancaster, S. Karsch, C.D. Murphy, P.A. Norreys, R.G. Evans, M. Borghesi, L. Romagnani, M. Zepf, T. Norimatsu, Y. Toyama, R. Kodama, J. A. King, R. Snavely, K. Akli, B. Zhang, R. Freeman, S. Hatchett, A.J. MacKinnon, P. Patel, M.H. Key, C. Stoeckl, R.B. Stephens, R.A. Fonseca, L.O. Silva, Physical Review E 70 (4) (2004) 046414.

[61] D.P. Higginson, A. Link, A. Schmidt, J. Comput. Phys. 388 (2019) 439.

[62] G. Ming Feng, dedx-erpa/dedx Github Repository, https://github.com/dedx-erpa/ dedx/tree/8c0b05024339058f26a53b9a0851614c4d81ea5d. accessed: 01, 2024.

[63] P. Wang, T.M. Mehlhorn, J.J. MacFarlane, Physics of Plasmas 5 (8) (1998) 2977.

[64] W.H. Barkas, J.N. Dyer, H.H. Heckman, Physical Review Letters 11 (1) (1963) 26.

[65] F. Bloch, Annalen Der Physik 408 (3) (1933) 285.

[66] X. Ning, T. Liang, D. Wu, S. Liu, Y. Liu, T. Hu, Z. Sheng, J. Ren, B. Jiang, Y. Zhao, D. H.H. Hoffmann, X. He, D. Batani, Laser and Particle Beams (2022) 2022.

[67] L. Willingale, G.M. Petrov, A. Maksimchuk, J. Davis, R.R. Freeman, A.S. Joglekar, T. Matsuoka, C.D. Murphy, V.M. Ovchinnikov, A.G.R. Thomas, L. Van Woerkom, K. Krushelnick, Physics of Plasmas 18 (2011) 8.

[68] A.P.L. Robinson, Plasma Physics and Controlled Fusion 64 (10) (2022) 105014.

[69] A.P.L. Robinson, Plasma Physics and Controlled Fusion 65 (5) (2023) 055004.

[70] D. Margarone, O. Klimo, I. J. Kim, J. Prokůpek, J. Limpouch, T. M. Jeong, T. Mocek, J. Pšikal, H. T. Kim, J. Proška, K. H Nam, L. Štolcová, I. W. Choi, S. K. Lee, J. H. Sung, T. J. Yu, and G. Korn Phys. Rev. Lett. 109, 234801.

[71] Alden Curtis, Chase Calvi, James Tinsley, Reed Hollinger, Vural Kaymak, Alexander Pukhov, Shoujun Wang, Alex Rockwood, Yong Wang, Vyacheslav N. Shlyaptsev & Jorge J. Rocca Nature Communications volume 9, 2018, 1077.